Electronic Supplementary Material (ESI) for Green Chemistry.

Supplementary Information

Green Synthesis of High-Performance $LiFePO_4$ Nanocrystals in Pure Water

Jinxing Yang,[a,b] Zhaojin Li,[a,c] Tianjia Guang,[a,b] Minmin Hu,[a,b] Renfei Cheng,[a,b] Ruoyu Wang,[a,b] Chao Shi,[a] Jixin Chen,[a] Pengxiang Hou,[a] Kongjun Zhu,[d] and Xiaohui Wang*[a]

[a]Shenyang National Laboratory for Materials Science, Institute of Metal Research, Chinese Academy of Sciences, Shenyang 110016, China

[b]School of Materials Science and Engineering, University of Science and Technology of China, Shenyang 110016, China

[c]University of Chinese Academy of Sciences, Beijing 100049, China

[d]State Key Laboratory of Mechanics and Control of Mechanical Structures, Nanjing University of Aeronautics and Astronautics, Nanjing 210016, China

1. Supporting Notes

1.1 Discussion on crystal orientation

To determine the crystal orientation of $LiFePO_4$, the particles were first ultrasonically dispersed in ethanol and then dried on an amorphous silicon substrate. In contrast to the as-synthesized $LiFePO_4$ powder with random orientation, the dispersed sample exhibits a strong [100] and [010] texture (Fig. S8a), which is apparently indicated by the decrease of $I_{(020)}/I_{(200)}$ from 2.9 in the as-synthesized powder to 1.5 in the dispersed sample. The degree of [100] and [010] texture was quantified using the Lotgering factor, f, which is defined by:[1]

$$f = (p - p_0)/(1 - p_0) \tag{1}$$

Where, an oriented sample (value p) and for the non-oriented material (value p_0), $p = \sum I_{h00}/\sum I_{hkl}$ or $p = \sum I_{0k0}/\sum I_{hkl}$ for the dispersed sample and $p_0 = \sum I_{h00}/\sum I_{hkl}$ or $p_0 = \sum I_{0k0}/\sum I_{hkl}$ for the as-synthesized powder. The Lotgering factor value for the dispersed sample is f_{100} = 20.8% and f_{010} = 27.1% respectively. The strong [100] and [010] texture in the dispersed sample implies that the O-$LiFePO_4$ nanocrystals have both [100] and [010] orientations, which is further confirmed by selected-area electron diffraction (SAED), as shown in Fig. S8b and c. The $LiFePO_4$ nanocrystals have both [100] and [010] orientations. It can be seen from TEM morphology that the $LiFePO_4$ nanocrystals present two different morphologies, i.e., hexagons and rectangles. The rectangular shape of $LiFePO_4$ particles show [100] orientation, while the hexagonal shape of $LiFePO_4$ nanocrystals show [010] orientation. This is because the nanocrystals are projected in different directions as shown in Fig. S8d–f. According to Islam and coworkers,[2] the relaxed surface energies of $LiFePO_4$ (100), (010), and (001) are 0.87, 0.72 and 1.11 J m^{-2}, respectively. Since the surfaces of (100) and (010) are small and close, it is easier to form [100] and [010] orientations. Thus, the size in both orientations is similar.

1.2 Discussion on EIS

Having firmly established the relevance of excellent electrochemical performance of O-$LiFePO_4$/C and R-$LiFePO_4$/C to lithium ion diffusion coefficient, electrochemical impedance spectroscopy (EIS) is adopted to gain insight into the electrochemical kinetic behavior and the interfacial properties between electrode and electrolyte. The Nyquist plots of $LiFePO_4$ nanomaterials show two different parts, a loop at high-frequency regions followed by a sloping line at low-frequency regions (Fig. S14a). The high frequency semicircle corresponds to the charge transfer resistance R_{ct} between the electrode and electrolyte, while the low-frequency oblique line indicates the Warburg impedance (Z_W), which is attributed to the Li^+ diffusion in the electrode materials. According to the equivalent circuit (Fig. S15a), the values of above indicators are displayed in Table S2, from which we can see that the indicators for electrochemical kinetic behavior and the interfacial properties between electrode and electrolyte are comparable for O-$LiFePO_4$/C and R-$LiFePO_4$/C. Additionally, the D_{Li^+} of the $LiFePO_4$/C samples can be calculated according to the equation[3]

$$D_{Li^+} = \frac{R^2T^2}{2A^2n^4F^4C_0^2\sigma^2} \qquad (2)$$

where R is the gas constant, T the absolute temperature (298 K), F the Faraday constant and σ the Warburg factor associated with Z_{re} by the equation[3]

$$Z_{re} = K + \sigma\omega^{-1/2} \qquad (3)$$

According to the above equations, the D_{Li^+} were calculated to be 6.6×10^{-15} and 6.3×10^{-15} cm^2 s^{-1} for O-$LiFePO_4$/C and R-$LiFePO_4$/C samples, respectively.

2. Supporting Figures

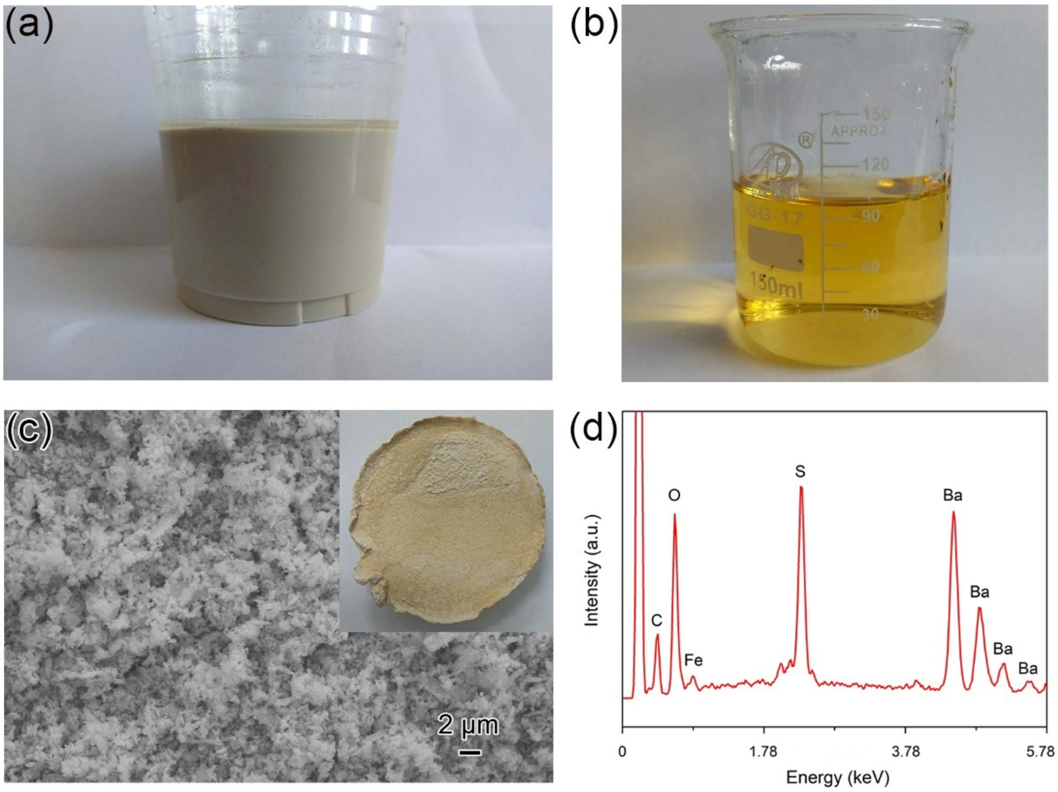

Fig. S1. As-synthesized suspension sample and the filtrate separated from the suspension. Photograph of (a) as-synthesized sample and (b) the filtrate. (c) SEM image of $BaSO_4$ precipitate. Inset shows the photograph of filter cake containing most of $BaSO_4$ precipitate. (d) EDS spectra of $BaSO_4$ precipitate, indicating that the presence of minor iron species.

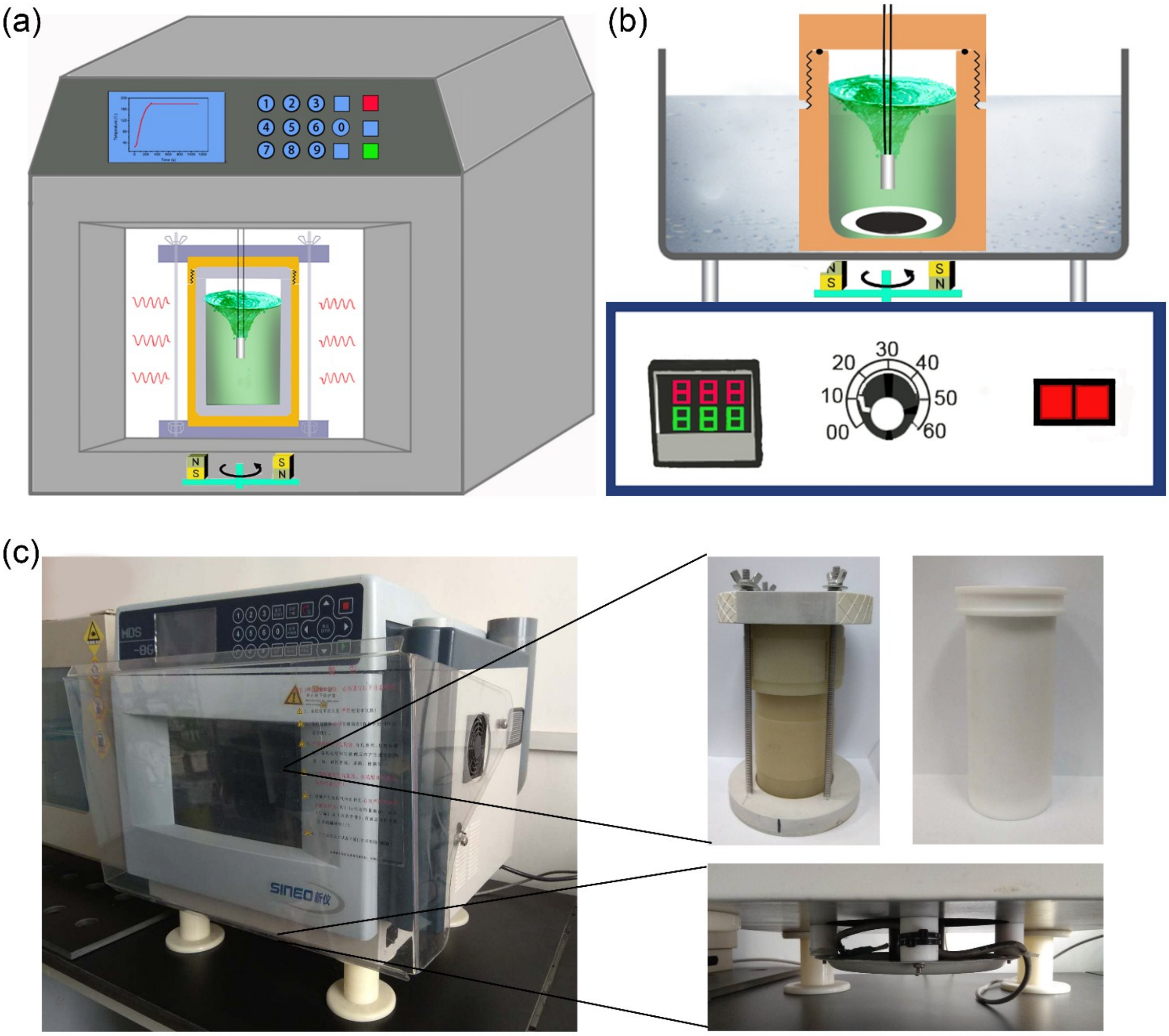

Fig. S2. Illustration of two different heating methods. (a) Microwave heating and (b) oil bath heating. (c) Photograph of microwave workstation. The reaction vessel is 100 mL-capacity Teflon autoclave whose top and bottom are reinforced with microwave-transparent ceramic components. Moreover, a stirring function was supplemented at the bottom of microwave workstation.

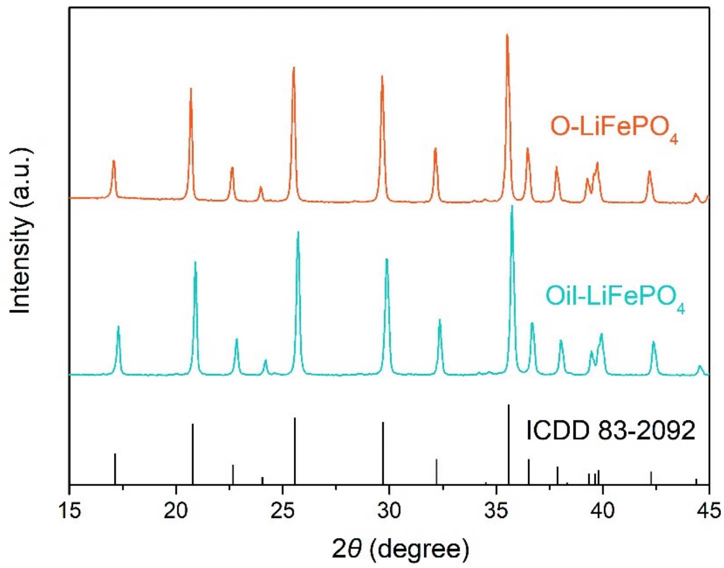

Fig. S3. XRD patterns of $LiFePO_4$ synthesized by (a) microwave heating and (b) oil bath heating.

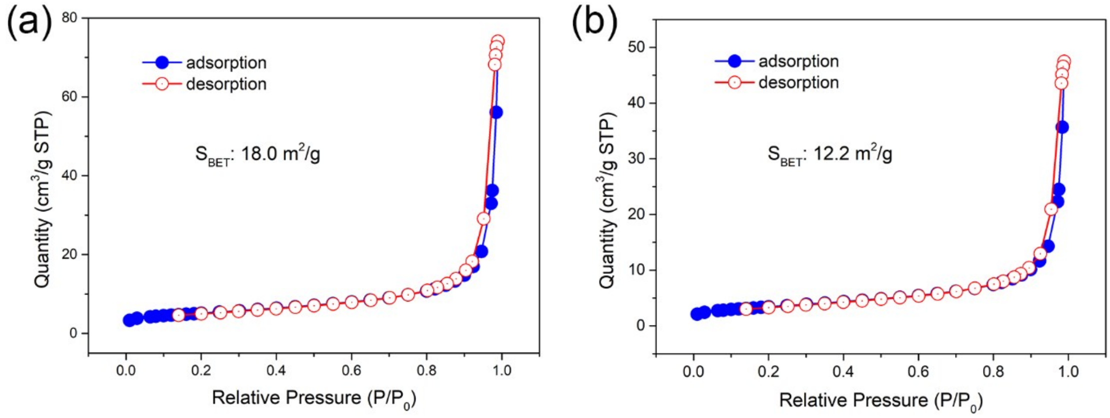

Fig. S4. Adsorption isotherms of $LiFePO_4$ samples by two different heating methods. The adsorption isotherms were analyzed and used to calculate the specific surface area (SSA) using the BET equation. P/P_0 values between 0.05 and 0.2 were used to calculate the SSA via multi-point BET. The slight hysteresis loop ($0.8 < P/P_0 < 1$) indicates the presence of macro-pores. The calculated SSA of (a) O-$LiFePO_4$ is 18.0 $m^2\ g^{-1}$, (b) Oil-$LiFePO_4$ is 12.2 $m^2\ g^{-1}$.

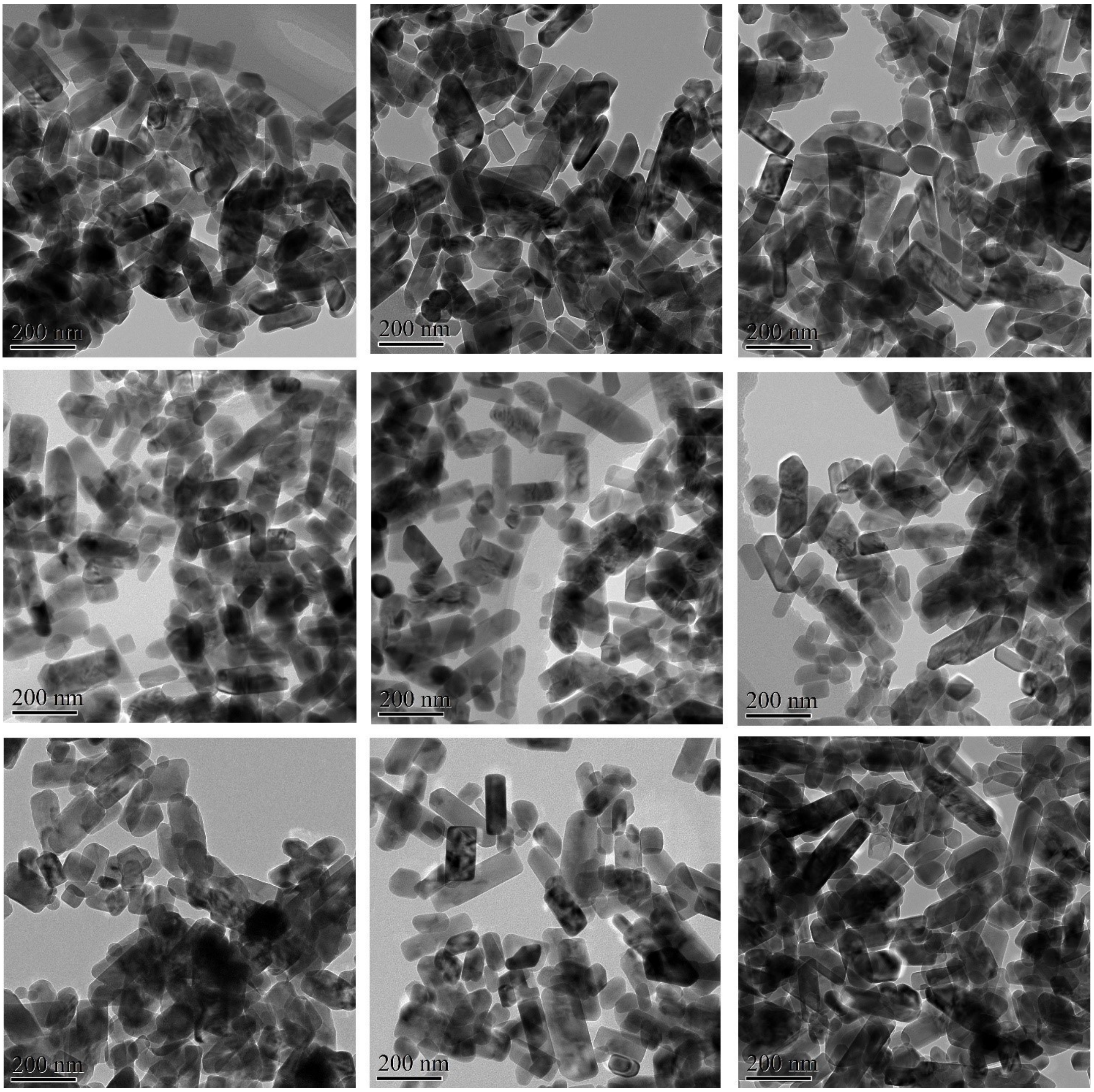

Fig. S5. Selected TEM images of O-$LiFePO_4$ nanocrystals synthesized by microwave heating for sizes statistics.

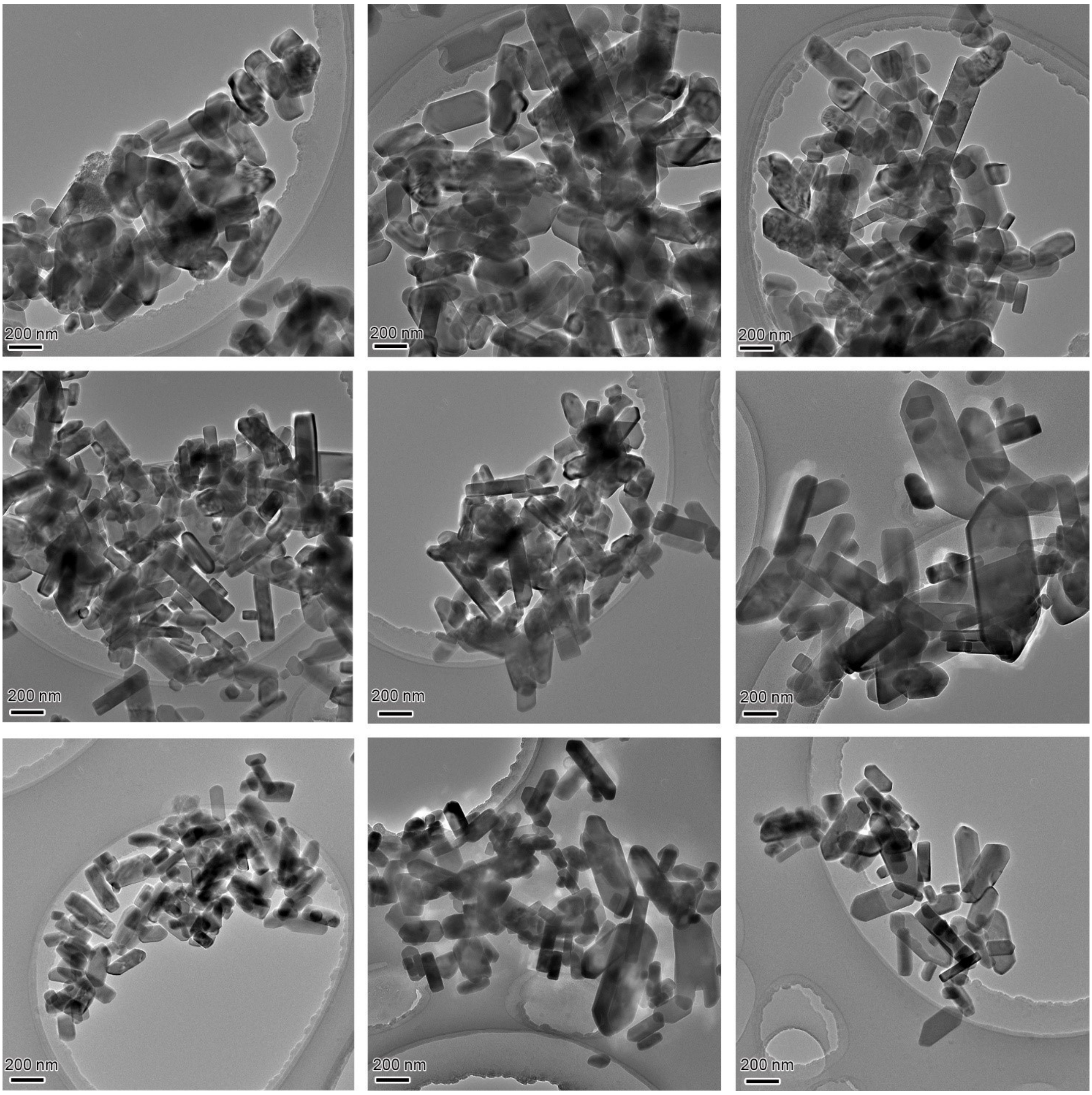

Fig. S6. Selected TEM images of $LiFePO_4$ nanocrystals synthesized by oil bath heating for sizes statistics.

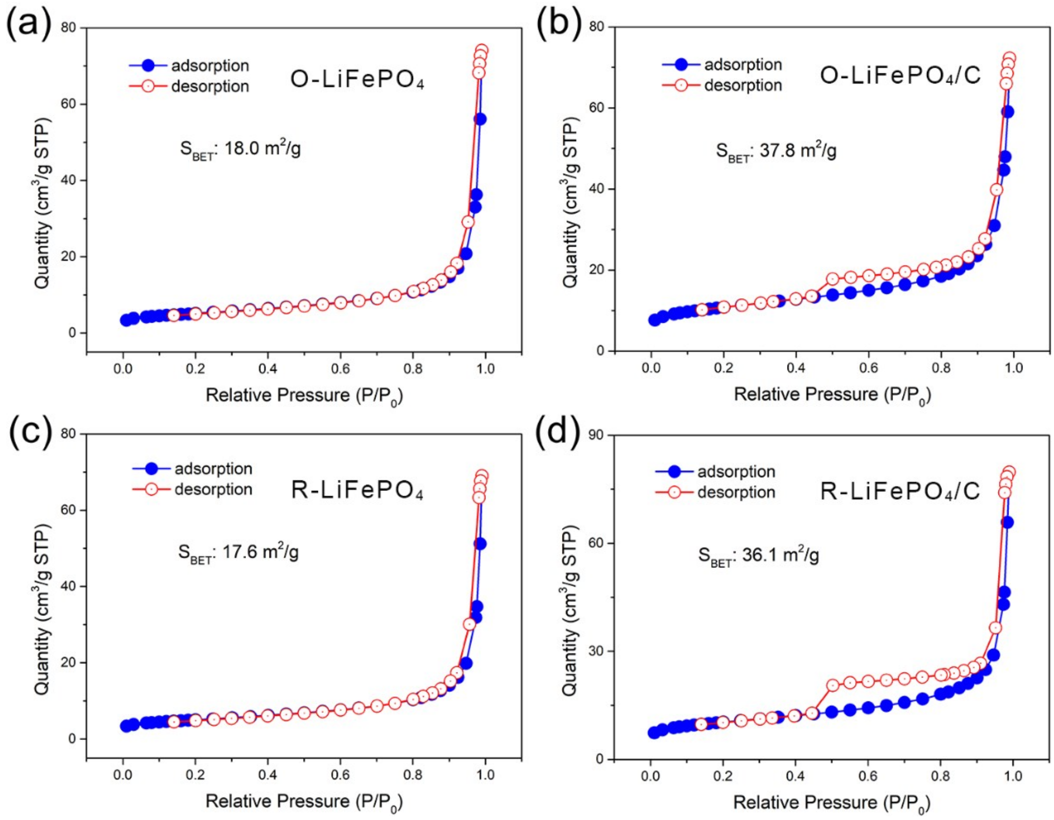

Fig. S7. Adsorption isotherms of O-$LiFePO_4$ and R-$LiFePO_4$ samples. The adsorption isotherms were analyzed and used to calculate the SSA using the BET equation. P/P_0 values between 0.05 and 0.2 were used to calculate the SSA via multi-point BET. The slight hysteresis loop ($0.4 < P/P_0 < 1$) indicates the presence of meso- and macro-pores for (b) O-$LiFePO_4$/C and (d) R-$LiFePO_4$/C. The calculated SSA of (a) O-$LiFePO_4$ is 18.0 m^2 g^{-1}, (b) O-$LiFePO_4$/C is 37.8 m^2 g^{-1}, (c) R-$LiFePO_4$ is 17.6 m^2 $g^{-1}$and (d) R-$LiFePO_4$/C is 36 .1 m^2 g^{-1}.

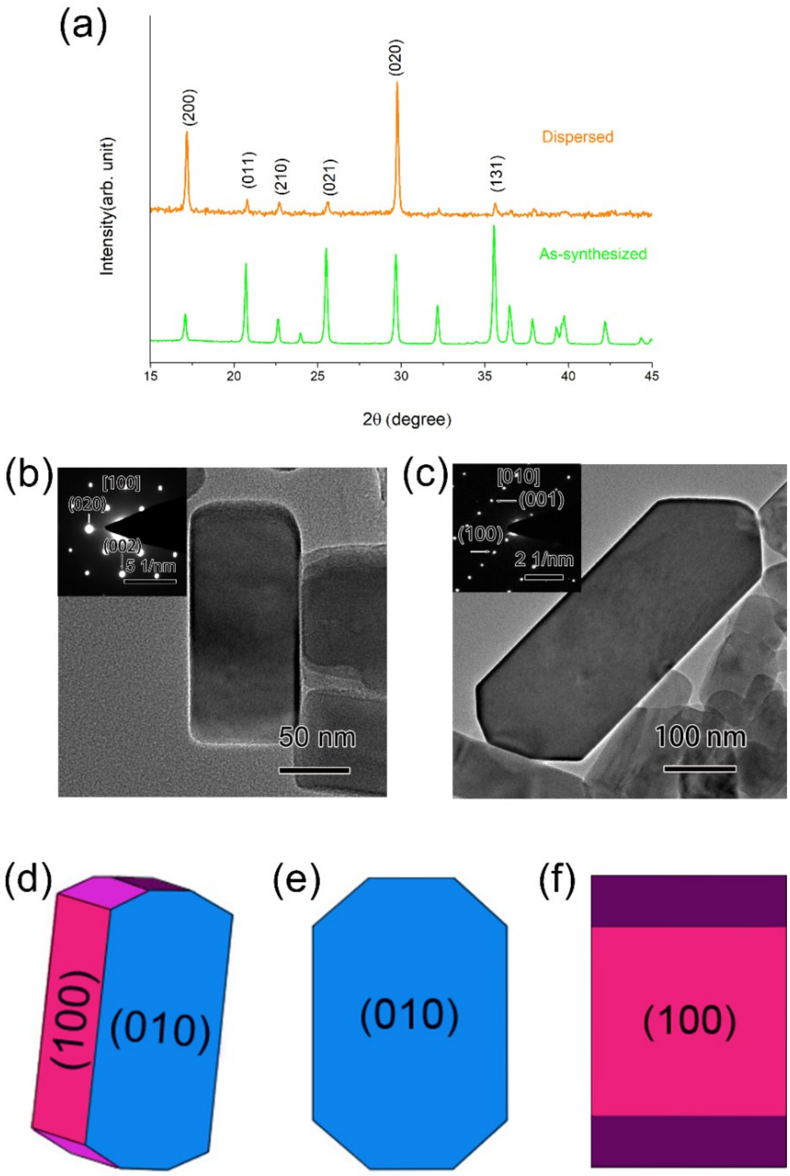

Fig. S8. Crystal orientation determination of O-$LiFePO_4$. (a) XRD patterns of the as-synthesized O-$LiFePO_4$ crystals and those first dispersed in ethanol and then slowly dried on an amorphous silicon substrate. (b) TEM morphology of the O-$LiFePO_4$ with rectangular geometry and the corresponding SAED pattern, indicating that the predominantly exposed facet is (100). (c) TEM morphology of the O-$LiFePO_4$ with hexagonal geometry and the corresponding SAED pattern, indicating that the predominantly exposed facet is (010). (d) Diagrammatic drawing of $LiFePO_4$ and its projections along (e) the [010] and (f) the [100] direction.

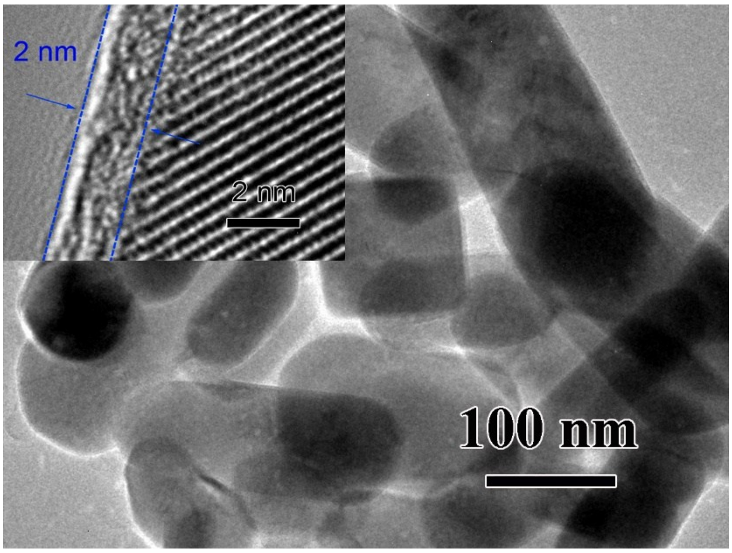

Fig. S9. TEM images of O-$LiFePO_4$/C. Inset shows carbon film coated on O-$LiFePO_4$/C.

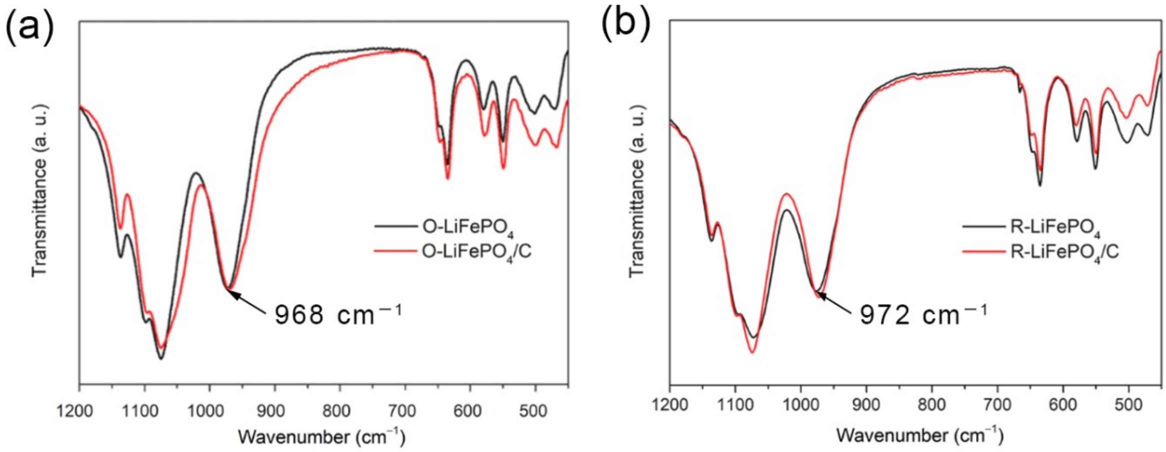

Fig. S10. FTIR spectra of the samples for (a): O-$LiFePO_4$, O-$LiFePO_4$/C and (b): R-$LiFePO_4$, R-$LiFePO_4$/C.

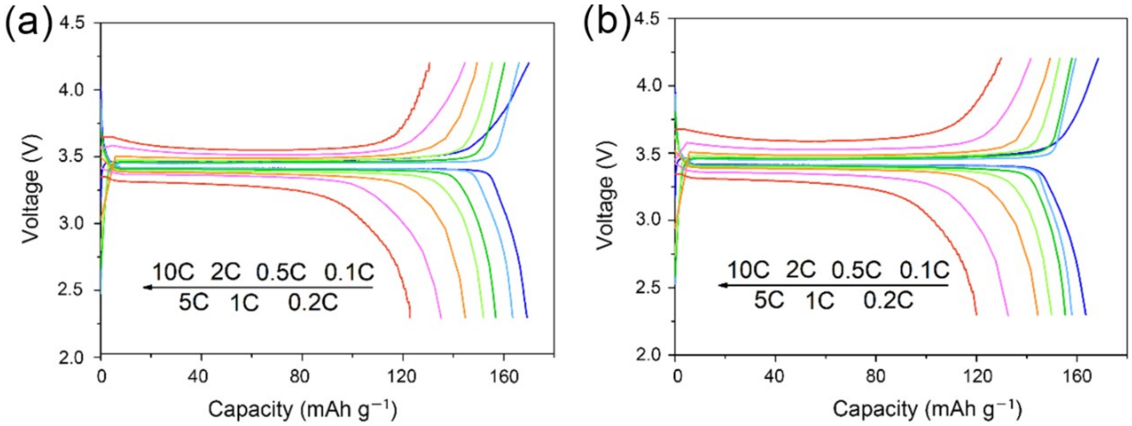

Fig. S11. Typical charge/discharge profiles of (a) O-$LiFePO_4$/C and (b) R-$LiFePO_4$/C.

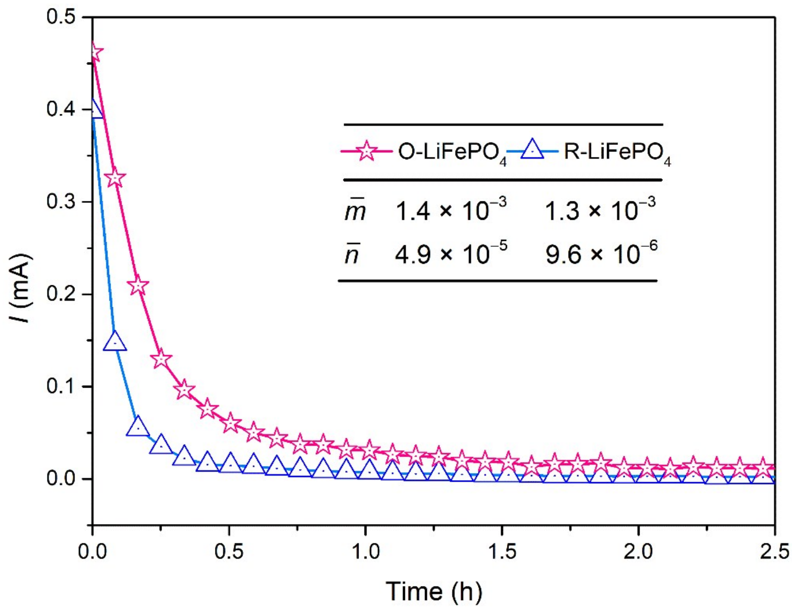

Fig. S12. Fitting results of the PITT experimental data of O-$LiFePO_4$/C and R-$LiFePO_4$/C. The coefficients of determination for O-$LiFePO_4$/C is R^2 = 0.9928 at a step of 150 mV, while for R-$LiFePO_4$/C is R^2 = 0.9507 at a step of 150 mV.

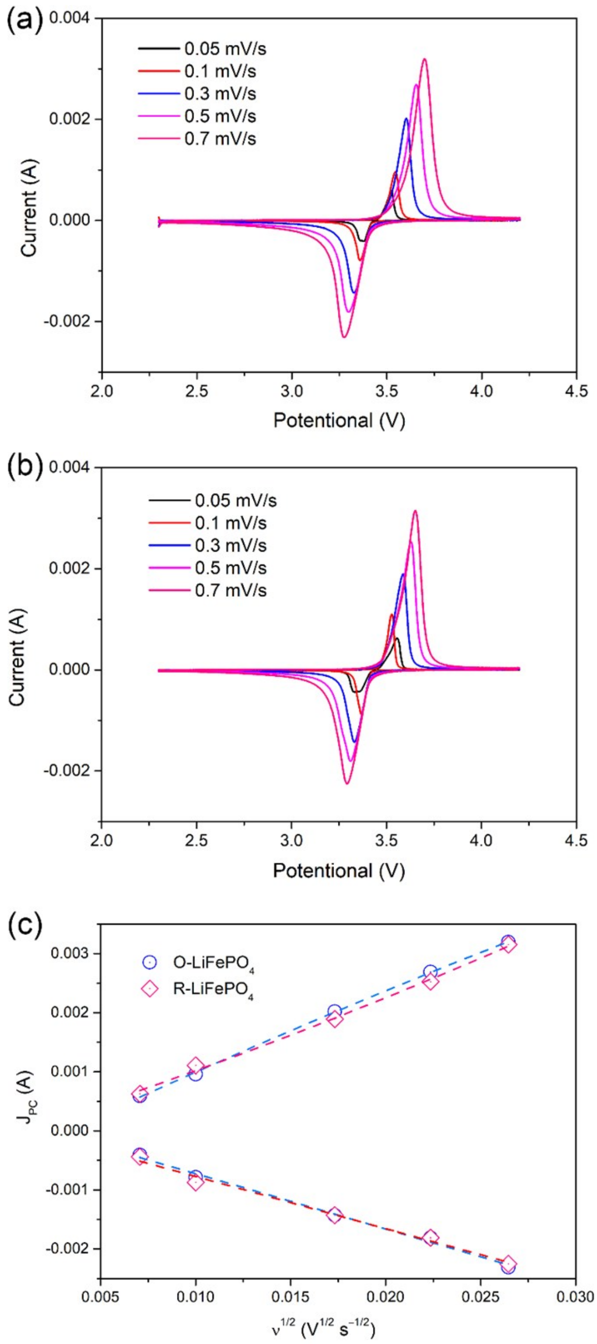

Fig. S13. CV profiles of the (a) O-$LiFePO_4$/C and (b) R-$LiFePO_4$/C at various sweeping rates of 0.05, 0.1, 0.3, 0.5, and 0.7 mV s^{-1}. (c) Peak current density as a function of the square root of the scanning rate derived from the sweeping-rate-dependent CV profiles.

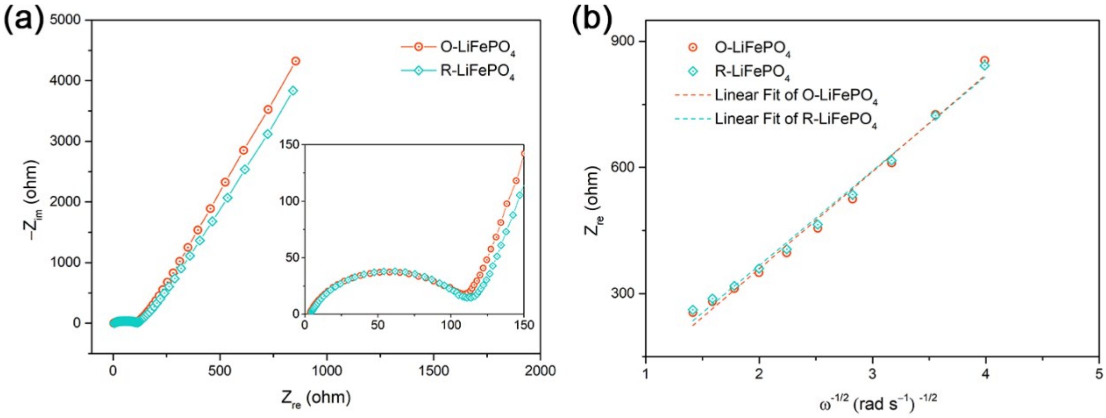

Fig. S14. EIS spectra of O-$LiFePO_4$/C and R-$LiFePO_4$/C. (a) Nyquist impedance spectra of O-$LiFePO_4$/C and R-$LiFePO_4$/C at room temperature and (b) Linear fittings between Z_{re} and the reciprocal of the square root of the angular frequency in the low frequency region. The real part of the Warburg impedance (Z_{re}) versus the square root of frequency ($\omega^{-1/2}$) at open circuit voltage for the O-$LiFePO_4$/C and R-$LiFePO_4$/C.

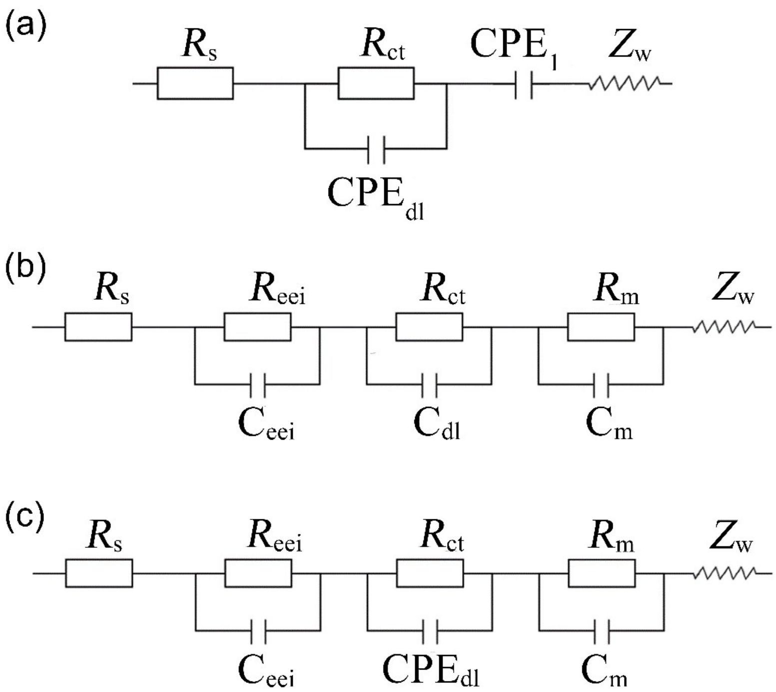

Fig. S15. Equivalent circuit of EIS spectra. Equivalent circuit adopted in the simulation of EIS spectra for (a) O-$LiFePO_4$/C and R-$LiFePO_4$/C electrodes. R_s: electrolyte resistance; CPE_{dl}: electrical double layer capacitor; R_{ct}: charge transfer resistance; CPE_1: constant phase angle element and Z_w: Warburg impedance. (b) and (c) O-$LiFePO_4$/C at redox voltages. R_{eei}: the interface resistance between electrode and electrolyte; R_m: the migration of Li^+ ions in the electrode.

3. Supporting Tables

Table S1. Compare the volume specific yield of $LiFePO_4$ that was prepared by hydro(solvo)thermal synthesis. H: hydrothermal, S: solvothermal.

Year	Method	Raw materials	Morphology	Size	Yield (mol/L)	Ref.
2010	H	$LiOH \cdot H_2O$ $FeSO_4 \cdot 7H_2O$ H_3PO_4	Platelike	1–2 μm	0.56	4
2011	S	LiOH $FeSO_4$ H_3PO_4	Quasi-spherical	2–5 μm	0.10	5
2012	H	$LiOH \cdot H_2O$ $FeSO_4 \cdot 7H_2O$ H_3PO_4 SDBS	Nanoplates Nanorods	width: 50 nm, *b*: 20 nm; *b*: 90 nm length: 200 nm–1 μm	0.38	6
2012	S	Li_2SO_4 $Fe(NO_3)_3 \cdot 9H_2O$ P_2O_5	Microspheres	1.6 μm	0.17	7
2013	S	$LiOH \cdot H_2O$ $FeSO_4 \cdot 7H_2O$ H_3PO_4	Agglomeration	300–500 nm	0.15	8
2013	H	$LiOH \cdot H_2O$ $FeSO_4 \cdot 7H_2O$ $NH_4H_2PO_4$ PVP $Na_4P_2O_7 \cdot 10H_2O$	Ellipsoid Spindle Sheet Plate Nanoparticle	300–500 nm 500 nm–2 μm, width: 100 nm 300 nm 100 nm	0.08	9
2013	H	$LiOH \cdot H_2O$ $FeSO_4 \cdot 7H_2O$ H_3PO_4	Hexahedron	200 nm	0.33	10
2013	H	$LiOH \cdot H_2O$ $FeSO_4 \cdot 7H_2O$ H_3PO_4	Particles	150 nm	0.33	11
2013	S	LiH_2PO_4 $FeSO_4 \cdot 7H_2O$ DMAC	Flower-like	10 μm	1.00	12
2013	S	$LiOH \cdot H_2O$ $FeSO_4 \cdot 6H_2O$ H_3PO_4	Nano-particles	80 nm, 30 nm	0.20	13
2013	S	LiOH $FeCl_2 \cdot 4H_2O$ H_3PO_4	hollow spheres	1 μm	0.40	14
2014	H	$LiOH \cdot H_2O$ $FeSO_4 \cdot 7H_2O$ H_3PO_4	Plate Spheroidal	350 nm 100–150 nm	0.11	15
2014	H	$CH_3COOLi \cdot 2H_2O$ $Fe(NO_3)_3 \cdot 9H_2O$ $NH_4H_2PO_4$	Spherical	2–4 μm	0.67	16
2014	H	LiOH $FeSO_4 \cdot 7H_2O$ H_3PO_4	(001) Microplate, (010) Microplate	11.8 μm 2.3 μm	1.00	17
2014	H	LiOH $FeSO_4 \cdot 7H_2O$ H_3PO_4	Particles	50–200 nm	0.80	18
2014	H	LiOH $FeSO_4$ H_3PO_4	Nanoparticles	50–150 nm	0.20	19
2014	S	LiH_2PO_4 $FeCl_2 \cdot 4H_2O$	Nanowires	5 μm, 40 nm	0.15	20

2014	S	$LiOH·H_2O$ $FeSO_4·7H_2O$ H_3PO_4	Nanoplates Nanorods	100–150 nm, 100 nm 250 nm, 40 nm	0.30	21
2014	S	$LiOH·H_2O$ $FeSO_4·7H_2O$ H_3PO_4	Nanoplates Rectangular prism Hexagonal prism	＜100 nm *a*: 100 nm 100 nm	0.38	22
2014	S	$LiCl·H_2O$ $FeCl_3·6H_2O$ $NH_4H_2PO_4N_2H_4·H_2O$	Microplates Microflowers	length: 2.5 μm width: 1.5 μm, thickness :200–500 nm	0.21	23
2014	S	$LiOH·H_2O$ $FeSO_4·7H_2O$ H_3PO_4	Nanoplates	90–250 nm	0.20	24
2015	S	$CH_3COOLi·2H_2O$ $Fe(NO_3)_3·9H_2O$ $NH_4H_2PO_4$	Starfish-like	10 μm	0.27	25
2015	H	$LiOH·H_2O$ $Fe(NO_3)·9H_2O$ $NH_4H_2PO_4$	Spherical	4 μm	0.25	26
2015	H	Li_2CO_3 $(NH_4)_2Fe(SO_4)_2·6H_2O$ $(NH_4)_2HPO_4$	Spherical-like Cubic	200–500 nm 200–500 nm	0.13	27
2015	S	$LiOH·H_2O$ $FeSO_4·7H_2O$ H_3PO_4	Nanoplates	50–100 nm	0.30	28
2015	S	$LiOH·H_2O$ $FeSO_4·7H_2O$ H_3PO_4	Ellipsoidal Platelet	230 nm, 160 nm. length and width 3 μm	0.11	29
2015	S	$LiOH$ $FeSO_4$ H_3PO_4	Nanorods	length: 50–100 nm, width: 30–50 nm	0.03	30
2015	S	$LiOH·H_2O$ $FeSO_4·7H_2O$ H_3PO_4	Hollow nanoparticles	150–300 nm	0.14	31
2015	S	$LiOH·H_2O$ $FeSO_4·7H_2O$ H_3PO_4 Tween-80	Rod-like	830 nm	0.50	32
2015	S	$LiOH·H_2O$ $FeSO_4·7H_2O$ H_3PO_4	Spindle-like	long axis: 650 nm short axis: 300 nm	0.80	33
2015	S	$LiOH·H_2O$ $FeSO_4·7H_2O$ H_3PO_4	Plates	thickness: 25 nm	0.38	34
2015	S	$LiOH·H_2O$ $FeSO_4·7H_2O$ H_3PO_4	Nanoplates	*a*, *b*, *c*: 60–80 nm, ~30 nm, 80–100 nm	0.25	35
2016	S	$LiOH·H_2O$ $FeSO_4·7H_2O$ H_3PO_4	Nanoflakes	*a*, *b*, *c*: 12, 134,	0.99	36

				280 nm		
2016	S	$LiOH·H_2O$ $FeSO_4·7H_2O$ H_3PO_4	Nanosheets	thickness: 50 nm	0.05	37
2016	H	$LiOH·H_2O$ $(NH_4)_2Fe(SO_4)_2·6H_2O$ $NH_4H_2PO_4$	Plat-form	0.5–1 μm	0.17	38
2016	S	$LiOH·H_2O$ $FeSO_4·7H_2O$ H_3PO_4	Plate-like	300 nm	0.13	39
2016	H	$LiOH·H_2O$ $FeSO_4·7H_2O$ H_3PO_4	Rectangular particles	width: 100–150 nm, length: 300–600 nm	0.33	40
2016	H	$LiOH·H_2O$ $FeSO_4·7H_2O$ H_3PO_4	Hexagonal hollow crystal	1–2 μm	0.40	41
2016	S	$LiOH·H_2O$ $FeSO_4·7H_2O$ H_3PO_4	Plates	thickness: 200 nm	0.40	42
2016	S	$LiOH·H_2O$ $FeSO_4·7H_2O$ H_3PO_4	Nanoflakes	150 nm	0.11	43
2016	S	$LiOH·H_2O$ $FeSO_4·7H_2O$ H_3PO_4	Nanorods	length: 90–150 nm, diameter: 70 nm	0.13	44
2016	S	$CH_3COOLi·2H_2O$ $Fe(NO_3)_3·9H_2O$ $NH_4H_2PO_4$	Nanoparticles Nanoplates	diameter: 200 nm thickness: ＜100 nm	0.25	45
2017	S	$LiOH·H_2O$ $FeSO_4·7H_2O$ H_3PO_4	Particles	80 nm	0.20	46
2017	S	$LiOH·H_2O$ $FeSO_4·7H_2O$ H_3PO_4	Rectangular shape	180 nm	0.30	47
2018	H	$LiOH·H_2O$ $FeSO_4·7H_2O$ H_3PO_4	Nanorods	*a*, *b*, *c*: 65, 62, 134 nm	1.32	this work

Table S2. Simulation results of the equivalent circuit in **Fig. S15(a)**.

Elements	**O-$LiFePO_4$/C**		**R-$LiFePO_4$/C**	
	Values	**Error/%**	**Values**	**Error/%**
$\boldsymbol{R_s}$ **(ohm)**	3.1	1.2	3.9	1.3
$\boldsymbol{R_{ct}}$ **(ohm)**	102.4	0.8	105.8	0.7
CPE_{dl} (F)	2.3×10^{-5}	3.0	1.5×10^{-5}	3.3
CPE_1 (F)	3.1×10^{-3}	1.8	3.5×10^{-3}	1.8
$\boldsymbol{Z_w}$ **(ohm)**	1.2×10^{-4}	7.6	1.3×10^{-4}	7.5

Table S3. Simulation results of the equivalent circuit in **Fig. S15(b) and (c)**.

Elements	Charge: 3.50 V		Charge: 3.55 V	
	Values	Error/%	Values	Error/%
R_s (ohm)	3.6	6.5	6.1	3.7
R_{eei} (ohm)	37.4	8.2	17.6	7.7
C_{eei} (F)	1.7×10^{-6}	4.7	5.6×10^{-4}	18.2
R_{ct} (ohm)	173.2	2.3	17.6	3.4
C_{dl}/CPE_{dl} (F)	5.1×10^{-4}	13.6	2.8×10^{-6}	8.5
R_m (ohm)	93.0	4.4	10.2	10.5
C_m (F)	4.0×10^{-6}	7.8	1.1×10^{-6}	6.8
Z_w (ohm)	2.0×10^{-2}	6.8	1.3×10^{-4}	7.5
Elements	**Discharge: 3.30 V**		**Discharge: 3.40 V**	
	Values	**Error/%**	**Values**	**Error/%**
R_s (ohm)	5.9	5.3	4.8	2.1
R_{eei} (ohm)	24.8	6.9	4.0	5.7
C_{eei} (F)	5.0×10^{-6}	17.8	2.1×10^{-3}	13.3
R_{ct} (ohm)	37.1	8.0	29.1	1.5
C_{dl}/CPE_{dl} (F)	2.1×10^{-3}	17.8	1.6×10^{-5}	8.9
R_m (ohm)	12.4	12.8	1.6	15.2
C_m (F)	1.1×10^{-6}	8.4	2.2×10^{-6}	12.6
Z_w (ohm)	2.6×10^{-2}	5.7	3.6×10^{-2}	0.6

4. References

1. F. K. Lotgering, *J. Inorg. Nucl. Chem.*, 1959, **9**, 113–123.
2. C. A. J. Fisher and M. S. Islam, *J. Mater. Chem.*, 2008, **18**, 1209–1215.
3. L. L. Peng, X. Zhang, Z. W. Fang, Y. Zhu, Y. J. Xie, J. J. Cha and G. H. Yu, *Chem. Mater.*, 2017, **29**, 10526–10533.
4. X. Qin, X. Wang, H. Xiang, J. Xie, J. Li and Y. Zhou, *J. Phys. Chem. C*, 2010, **114**, 16806–16812.
5. X. Zhou, F. Wang, Y. Zhu and Z. Liu, *J. Mater. Chem.*, 2011, **21**, 3353–3358.
6. B. Pei, H. Yao, W. Zhang and Z. Yang, *J. Power Sources*, 2012, **220**, 317–323.
7. H. Deng, S. Jin, L. Zhan, Y. Wang, W. Qiao and L. Ling, *J. Power Sources*, 2012, **220**, 342–347.
8. D. Zhao, Y. L. Feng, Y. G. Wang and Y. Y. Xia, *Electrochim. Acta*, 2013, **88**, 632–638.
9. Y. Yu, Q. Li, Y. Ma, X. Zhang, Y. Zhu and Y. Qian, *J. Nanosci. Nanotechnol.*, 2013, **13**, 1515–1519.
10. J. Li, Q. Qu, L. Zhang, L. Zhang and H. Zheng, *J. Alloys Compd.*, 2013, **579**, 377–383.
11. Z. Chen, B. Du, M. Xu, H. Zhu, L. Li and W. Wang, *Electrochim. Acta*, 2013, **109**, 262–268.
12. N. Zhou, E. Uchaker, H. Y. Wang, M. Zhang, S. Q. Liu, Y. N. Liu, X. Wu, G. Cao and H. Li, *RSC Advances*, 2013, **3**, 19366–19374.
13. L. Wang, W. Sun, X. Tang, X. Huang, X. He, J. Li, Q. Zhang, J. Gao, G. Tian and S. Fan, *J. Power Sources*, 2013, **244**, 94–100.
14. S. Yang, M. Hu, L. Xi, R. Ma, Y. Dong and C. Y. Chung, *ACS Appl. Mater. Interfaces*, 2013, **5**, 8961–8967.
15. Z. Y. Chen, M. Xu, B. L. Du, H. L. Zhu, T. Xie and W. H. Wang, *J. Power Sources*, 2014, **272**, 837–844.
16. L. Y. Tan, Q. L. Tang, X. H. Chen, A. P. Hu, W. N. Deng, Y. S. Yang and L. S. Xu, *Electrochim. Acta*, 2014, **137**, 344–351.
17. Y. Q. Wang, D. Y. Zhang, C. K. Chang, L. Deng and K. J. Huang, *Mater. Chem. Phys.*, 2014, **148**, 933–939.
18. Y. Zhang, L. Wu, J. Zhao and W. Yu, *J. Electroanal. Chem.*, 2014, **719**, 1–6.
19. Y. Ma, X. L. Li, Z. Xie, Z. L. Xiu, Y. Z. Wu and X. P. Hao, *J. Mater. Sci.: Mater. Electron.*, 2014, **25**, 2716–2723.
20. L. Peng, Y. Zhao, Y. Ding and G. Yu, *Chem. Commun.* 2014, **50**, 9569–9572.

21. J. J. Song, L. Wang, G. J. Shao, M. W. Shi, Z. P. Ma, G. L. Wang, W. Song, S. Liu and C. X. Wang, *Phys. Chem. Chem. Phys.*, 2014, **16**, 7728−7733.
22. Z. P. Ma, G. J. Shao, Y. Q. Fan, G. L. Wang, J. J. Song and T. T. Liu, *ACS Appl. Mater. Interfaces*, 2014, **6**, 9236−9244.
23. J. Zhang, J. B. Lu, D. C. Bian, Z. H. Yang, Q. Wu and W. X. Zhang, *Ind. Eng. Chem. Res.*, 2014, **53**, 12209−12215.
24. M. M. Chen, Q. Q. Ma, C. Y. Wang, X. Sun, L. Q. Wang and C. Zhang, *J. Power Sources*, 2014, **263**, 268−275.
25. M. F. Chen, X. Y. Wang, H. B. Shu, R. Z. Yu, X. K. Yang and W. H. Huang, *J. Alloys Compd.*, 2015, **652**, 213−219.
26. W. Wei, L. Guo, X. Qiu, P. Qu, M. Xu and L. Guo, *RSC Advances*, 2015, **5**, 37830−37836.
27. X. F. Li, D. M. Luo, X. Zhang and Z. Zhang, *J. Power Sources*, 2015, **291**, 75−84.
28. J. J. Song, G. J. Shao, Z. P. Ma, G. L. Wang and J. Yang, *Electrochim. Acta*, 2015, **178**, 504−510.
29. Y. Li, J. N. Weker, W. E. Gent, D. N. Mueller, J. Lim, D. A. Cogswell, T. Tyliszczak and W. C. Chueh, *Adv. Funct. Mater.*, 2015, **25**, 3677−3687.
30. R. Y. Tian, H. Q. Liu, Y. Jiang, J. K. Chen, X. H. Tan, G. G. Liu, L. Zhang, X. H. Gu, Y. J. Guo, H. F. Wang, L. F. Sun and W. G. Chu, *ACS Appl. Mater. Interfaces*, 2015, **7**, 11377−11386.
31. Z. M. Zheng, W. K. Pang, X. C. Tang, D. Z. Jia, Y. D. Huang and Z. P. Guo, *J. Alloys Compd.*, 2015, **640**, 95−100.
32. Y. Y. Liu, J. J. Gu, J. L. Zhang, F. Yu, J. Wang, N. Nie and W. Li, *RSC Advances*, 2015, **5**, 9745−9751.
33. Y. P. Zhang, L. L. Wu, J. B. Zhao and W. Y. Yu, *Mater. Chem. Phys.*, 2015, **166**, 182−189.
34. Z. P. Ma, Y. Q. Fan, G. J. Shao, G. L. Wang, J. J. Song and T. L. Liu, *ACS Appl. Mater. Interfaces*, 2015, **7**, 2937−2943.
35. B. Wang, A. Liu, W. A. Abdulla, D. Wang and X. S. Zhao, *Nanoscale*, 2015, **7**, 8819−8828.
36. Z. Li, Z. Peng, H. Zhang, T. Hu, M. Hu, K. Zhu and X. Wang, *Nano Lett.*, 2016, **16**, 795−799.
37. S. Lin, Q. Ge, Y. Cao, W. Qin and X. Wen, *Mater. Express*, 2016, **6**, 351−356.
38. L. Yang, J. Chen, L. Chen, P. Yang, J. Zhang, A. Li, Y. Wang, Y. Wang and R. Wang, *J. Mater. Sci. Mater. Electron.*, 2016, **27**, 12258−12263.

39. L. Bao, L. L. Li, G. Xu, J. W. Wang, R. Y. Zhao, G. Shen, G. R. Han and S. X. Zhou, *Electrochim. Acta*, 2016, **222**, 685−692.
40. A. Milev, L. George, S. Khan, P. Selvam and G. S. Kamali Kannangara, *Electrochim. Acta*, 2016, **209**, 565−573.
41. A. Paolella, S. Turner, G. Bertoni, P. Hovington, R. Flacau, C. Boyer, Z. Feng, M. Colombo, S. Marras, M. Prato, L. Manna, A. Guerfi, G. P. Demopoulos, M. Armand and K. Zaghib, *Nano Lett.*, 2016, **16**, 2692−2697.
42. G. Liu, S. Zhang, X. Wei, S. Wang and Y. Yu, *Int. J. Electrochem. Sci.*, 2016, **11**, 6799−6807.
43. L. Hu, T. W. Zhang, J. W. Liang, Y. C. Zhu, K. L. Zhang and Y. T. Qian, *RSC Advances*, 2016, **6**, 456–463.
44. Y. J. Wang, B. Zhu, Y. M. Wang and F. Wang, *Ceram. Int.*, 2016, **42**, 10297−10303.
45. Y. Zhou, J. Lu, C. Deng, H. Zhu, G. Z. Chen, S. Zhang and X. Tian, *J. Mater. Chem. A*, 2016, **4**, 12065−12072.
46. X. Huang, X. He, C. Jiang, G. Tian and Y. Liu, *Ind. Eng. Chem. Res.*, 2017, **56**, 10648−10657.
47. X. Huang, K. Zhang, F. Liang, Y. Dai and Y. Yao, *Electrochim. Acta*, 2017, **258**, 1149−1159.